Surpassingly Competitive Electromagnetic Field Enhancement at the Silica/Silver Interface for Selective Intracellular Surface Enhanced Raman Scattering Detection

Darya Radziuk* **and Helmuth Möhwald**

Max-Planck Institute of Colloids and Interfaces, Department of Interfaces, D14476 Potsdam, Germany

ABSTRACT A thin plasmonic nanofilm is formed by preformed silver nanoparticles (30 nm) in the matrix of poly(vinyl alcohol) adsorbed on silica microparticles (1.5 μm) (SiO_2@Ag-PVA). By applying finite element method (FEM) analysis the surface enhanced Raman spectroscopy (SERS) enhancement factors (EFs) can reach 10^5 with higher values from 10^9 to 10^{11} in the silver layer of 5 nm thickness. Nanoparticles in the SiO_2@Ag-PVA nanofilm need at least 15 nm radius to exhibit SERS EFs greater than 10^7. High values of this enhancement at the silver/silica interface of spherical geometry can be reached faster by using a 532 nm compared to 785 nm excitation wavelength. By this approach different SERS spectral features can be distinguished between live fibroblasts with spread ("healthy" state) or round ("unhealthy" state) shapes. Characteristic features of secondary protein structures, detection of different acidic conditions and cholesterol with at least a 3-fold higher sensitivity are examined. Moreover, a greater amount of glucose (glucogen) and also tyrosine can be monitored in real time. This is important in identification of higher risk of diabetes as well as in several genetic metabolic disorders (*e.g.*, phenylketonuria, tyrosinaemia type II and tyrosinosis).

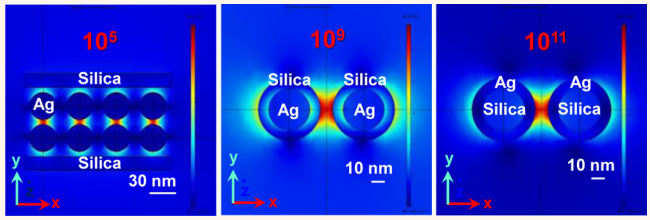

KEYWORDS: silica · silver · surface enhanced Raman scattering · intracellular · cell

Understanding how the compositional morphology of plasmonic nanostructures controls the properties of their surface plasmons is critical for the development of high-performance substrates for surface enhanced Raman spectroscopy (SERS). SERS requires nanoroughness of crevices, interparticle junctions (*i.e.*, hot spots as nanogaps <10 nm) and sharp edges of plasmonic materials with high electromagnetic field increase. We refer to the term "plasmonic" by meaning nanoparticles that exhibit surface plasmon resonance upon excitation by light (*e.g.*, silver, gold, cupper or alkali metals). At resonance Raman scattering is increased by surface Plasmon modes and depends on the nanoscale geometry (sphere, triangle, nanoegg, nanorice or nanocup, *etc.*),[1] composition (plasmonic or plasmonic-dielectric, *etc.*) and self-assembly.[2,3]

The SERS enhancement factors (EFs) at hot spots decrease by several orders of magnitude from 10^{11}–10^8 to 10^6–10^5 depending on the diameter of nanoparticles or nanotip at the distance from 1 to 2 to 10 nm.[4] However, little is known about the SERS EFs at the silica/silver interface of different geometrical curvature. So far, such studies are limited to a recent report on well-defined gold nanobridges, which contain silica as a separation layer (~1 nm).[5]

The key point in the elaboration of new colloidal SERS active platforms is their stability against uncontrolled aggregation, *i.e.*, strength and reliability of hot spots. Several approaches have been developed to control plasmonic nanogaps. One way is to isolate the nanoparticle core by a dielectric shell with thickness controlling the interparticle distance (*e.g.*, SHINERS).[6,7] The ultrathin silica coating keeps the nanoparticles

* Address correspondence to darya.radziuk@mpikg.mpg.de.

Received for review November 26, 2014 and accepted February 21, 2015.

Published online February 22, 2015
10.1021/nn506741v

from agglomerating, separates them from direct contact with the probed material and allows the nanoparticles to conform to different contours of substrates. As advantage SERS signals can be measured when nanoparticles are spread over nonmetallic (*e.g.*, semiconducting surface, Si) or organic (*e.g.*, orange peel) surfaces. However, the silica and alumina shells are not completely inert, being incompatible with a high pH environment (silica-shell) or with a low pH value (alumina).

The second approach is to use a polymeric matrix, which offers design flexibility (*e.g.*, porosity or coating density and controlled distance by varying the chain length), while the conformation of polymers (*i.e.*, nanogap dimensions) can be adjusted to a suitable pH value, in contrast to silica coating.[8] Polymer coating of plasmonic nanoparticles does not require the use of organic solvents or hazardous silanes, can be biocompatible and facilitate molecular diffusion. SERS spectra can be collected with a higher degree of reproducibility and signal-to-noise ratio. Plasmonic nanogaps can be well protected against low pH of solution or organic solvent (advantage over silica coating). The quality of strong SERS spectra can be controlled by the filling factor of nanoparticles, *i.e.*, the higher the filling factor the greater SERS performance.[9] Stimuli responsive polymers can be used to control the reverse dynamic assembly of nanogaps[10,11] *via* linking, coating and molecular permeation.[12,13] The sequential addition of phosphate, linker, polymer, streptavidin, Raman tag, and biotinylated affinity label can be carried out without purification through the judicious choice of binding strength, concentration, and molecular size. This strategy can be used to demonstrate the multiplexed labeling of cancer cells, surpassing commonly used fluorescence multiplexing.

Examples of plasmonic nanogaps in the polymeric matrix include polyvinylpyrrolidone (PVP)-Ag colloidal solution on poly(methyl methacrylate) (PMMA) slides and poly(vinyl alcohol) (PVA) fibers with Ag nanocrystals or Au nanorods embedded by electrospinning for SERS detection,[14−16] thin films consisting of Au nanoparticles (10−60 nm) with long-range ordering porous structure and nanoscale roughness,[17] synthetic Ag bacterial cellulose nanocomposites acting as natural sponges in water or ethanol for SERS detection of the amino acids L-phenylalanine, L-glutamin and L-histidine.[18] For a real application of SERS substrates some of them can be designed for trace chemical detection and include flexible "smart film" membranes composed of Au NPs embedded in natural rubber[19] and cellulose-based dipsticks.[20] Reproducible SERS EFs can vary from 10^4 to 10^{10}.

We recently introduced a thin SERS active film consisting of preformed Ag nanoparticles in the polymeric matrix of polyethylene glycol[21] or poly(acrylic acid) adsorbed on larger silica microparticles.[22] The strength of plasmonic nanogaps can be controlled by the chain length of polymer and also by the formation of primary and secondary hot spots over the larger underlying substrate. The colloidal stability of nanogaps is due to the electrosteric interactions between the silver/polymer interfaces at the nano- or microscale. By this approach molecular signatures of live NIH3T3 fibroblasts can be intensified in real time allowing reliable SERS spectra for chemical imaging analysis.[22] Intracellular compartments can be distinguished by this approach excluding fluorescence labeling. However, the SERS spectra from nucleus, its periphery membrane and cytoplasm are averaged over the entire cell. Although the SERS EFs can reach 10^8 (sufficient for single molecule detection) the collected SERS spectra arise from the random distribution of EFs.

To understand the SERS enhancement in our approach we calculated for the first time the electromagnetic field increase at the silica/silver interface of various geometric curvatures (radii) and sequence of dielectric and metal properties and investigated it at different interparticle distances by the finite element method (FEM) (Scheme 1). Our "thin film" approach has been extended by the newly formed plasmonic film consisting of preformed silver−boron nanoparticles in the matrix of poly(vinyl alcohol) (Scheme 1). PVA is a nontoxic and water-soluble synthetic polymer with good film-forming ability used in many applications from drug delivery systems to membrane preparation.[23] Its bioinertness and biocompatibility allow medical applications (*e.g.*, artificial pancreas, hemodialysis, nanofilteration, synthetic vitreous and implantable medical device).[24−26] The intracellular studies of live fibroblasts have been advanced by SERS spectral differentiation of spread ("healthy") or round ("unhealthy") cells in real time. The difference of SERS spectra by two widely used excitation wavelengths (532 or 785 nm) has been demonstrated for the first time.

RESULTS AND DISCUSSION

Formation of SiO_2@Ag-PVA Nanofilms. The thin plasmonic nanofilm is composed of preformed silver−boron nanoparticles in a matrix of polyvinyl vinyl alcohol (Ag-PVA) (Figure 1A). The TEM image shows a majority of Ag-PVA NPs of spheroidal shape and diameter 33 ± 8 nm, although smaller NPs are also present (<10 nm). White arrows indicate the interparticle nanogaps (<10 nm) in the Ag-PVA matrix. The surface of Ag-PVA NPs can be chemically introduced as depicted on the schematics on the left in Figure 1A. In details, before coating with PVA the metallic silver core bears negative charge due to the presence of borohydride anions (BH_4^-). PVA can electrostatically coat bare Ag NPs with hydroxyl groups (OH^-) pointing outward the polymeric chain into closer interaction with water molecules.[34]

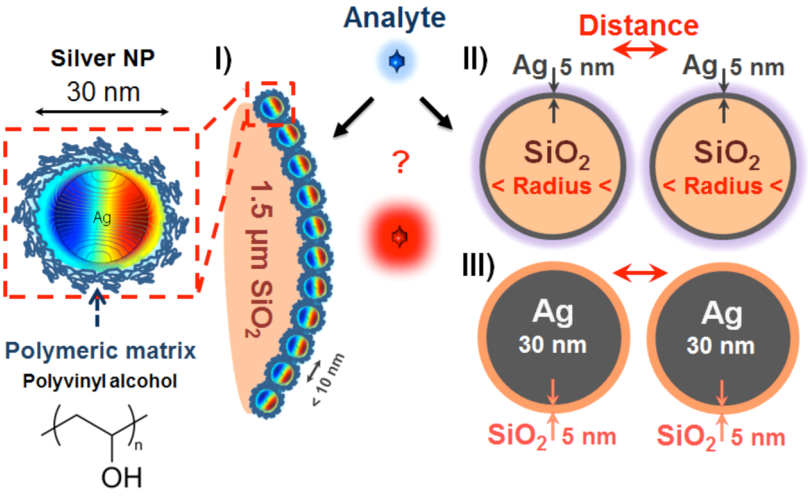

Scheme 1. Schematic illustration of the silica/silver interface with various curvature and sequence of dielectric and plasmonic properties, introduced by three models (I, II and III) for the surface enhanced Raman scattering (SERS) detection of an analyte. In the first model I preformed silver nanoparticles (30 nm) are embedded in the matrix of polyvinyl vinyl alcohol (PVA) and adsorbed on colloidal silica microparticles (1.5 μm). The second model II is introduced by the silica particles with a thin outer silver layer (5 nm) with varied radius and interparticle distances. The third model III is a reverse model II, in which the core is silver particle and the outer shell is a thin silica layer (5 nm).

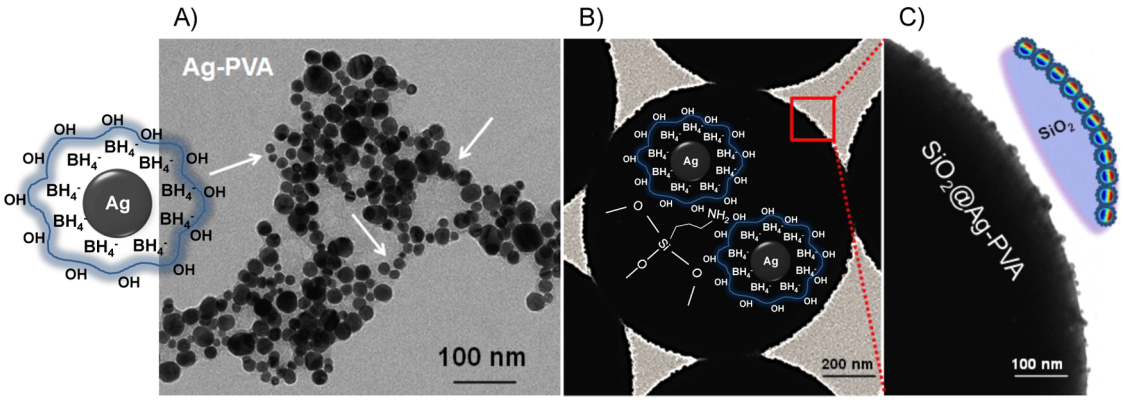

Figure 1. TEM images of (A) preformed silver−boron nanoparticles in the matrix of poly(vinyl alcohol) (Ag-PVA) in water (scale bar is 100 nm), (B) silica microparticles with adsorbed Ag-PVA nanoparticles (scale bar is 200 nm) and (C) magnified part of the silica surface with adsorbed Ag-PVA nanofilm (scale bar is 100 nm). Two insets show sketches of preformed Ag NPs in the matrix of PVA as (A) colloidal solution or (B and C) adsorbed on the surface of silica microparticles. The PVA matrix is introduced by a blue line with terminating hydroxyl groups pointing out for interaction with water molecules in the bulk.

This is due to the presence of loosely bonded protons in OH^-, NH^- or SH^- groups because hydrogen atoms attached to carbon will not be exchanged. The rate and extent of the exchange reaction will strongly depend on the mechanical and thermal history of the polymer. This we will take into account by applying laser excitation intensity as low as possible in order to avoid thermal defects (amorphization or destruction) of the Ag-PVA nanofilm in Raman measurement.

The ζ-potential of freshly formed Ag-PVA NPs was negative (-17 ± 2 mV) and no sediment was observed within weeks. It is important to note that the PVA matrix protects preformed Ag-boron NPs against attraction after heating at 37 or 70 °C (Figure S1, Supporting Information). The full width at half maximum (fwhm) of the UV−vis absorbance spectra of Ag-PVA NPs does not change much being 66 ± 1 nm with a constant peak position near 390 nm. In contrast, as a control experiment, the UV−vis absorbance band of bare Ag-boron NPs red shifts near 406 nm followed by broadening (fwhm = 90 ± 2 nm) after heating at 37 or 70 °C.

To remind, PVA is a nontoxic, water-soluble synthetic polymer with suitable physical and chemical properties and film-forming ability.[23] Moreover, PVA can reduce the unreacted Ag^+ ions into Ag nanoparticle due to the hydroxyl groups on the polymer backbone resulting in higher stabilization of nanoparticles against aggregation.[35] As there is a competition between the citrate ions and PVA to solubilize and/or incorporate into the Stern layer by electrostatic or chemical forces we used borate ions instead of citrate for silver nanoparticle formation. Moreover, PVA−OH groups have the ability to coordinate Ag^+ ions and its

nanoparticles, providing a favorable microenvironment for their capping. PVA forms an ion-pair complex between the lone pairs of the PVA HO-group and Ag^+ ions. As a result, the reduction of Ag^+ into Ag^0 can be inhibited but not totally prevented, which in turn decreases the nucleation rates and reduces the concentration of the unreacted ions. Inside the polymeric matrix silver ions can be reduced by the OH groups of PVA by a possible mechanism taking into account the secondary alcohol groups, R_2CHOH for polymer: $R_2CHOH + 2AgNO_3 \rightarrow R_2C = O + 2HNO_3 + 2Ag$ (R indicates the alkyl group).[36]

As the next step the Ag-PVA NPs were adsorbed on the surface of positively charged silica microparticles (MPs, 1.55 ± 0.04 μm) (Figure 1B). Prior NP adsorption the initial negative surface charge of SiO_2 MPs was reversed to a positive value by the procedure described elsewhere (Figure S2A).[28−30] After Ag NP adsorption the ζ-potential of SiO_2@Ag-PVA MPs was reversed to −15 ± 5 mV (pH = 8.8). Electron microscopy images show Ag-PVA nanofilm adsorbed on the colloidal silica surface (Figure 1C and Figure S2B), confirmed also by the UV−vis absorbance spectra (Figure S3).

Calculation of the Electromagnetic Field Enhancement (FEM). Before measurements of SERS we need to understand the distribution of the electric field component in the scattered field in our SiO_2@Ag-PVA MPs and find out parameters responsible for the electromagnetic field enhancement (*i.e.*, radius of the curvature and interparticle distance, Scheme 1). As the first step, we model Ag-PVA nanofilm adsorbed on a silica microsphere (1.5 μm) (Figure 2A−C, model I in Scheme 1). In this model the incident electromagnetic plane wave excites

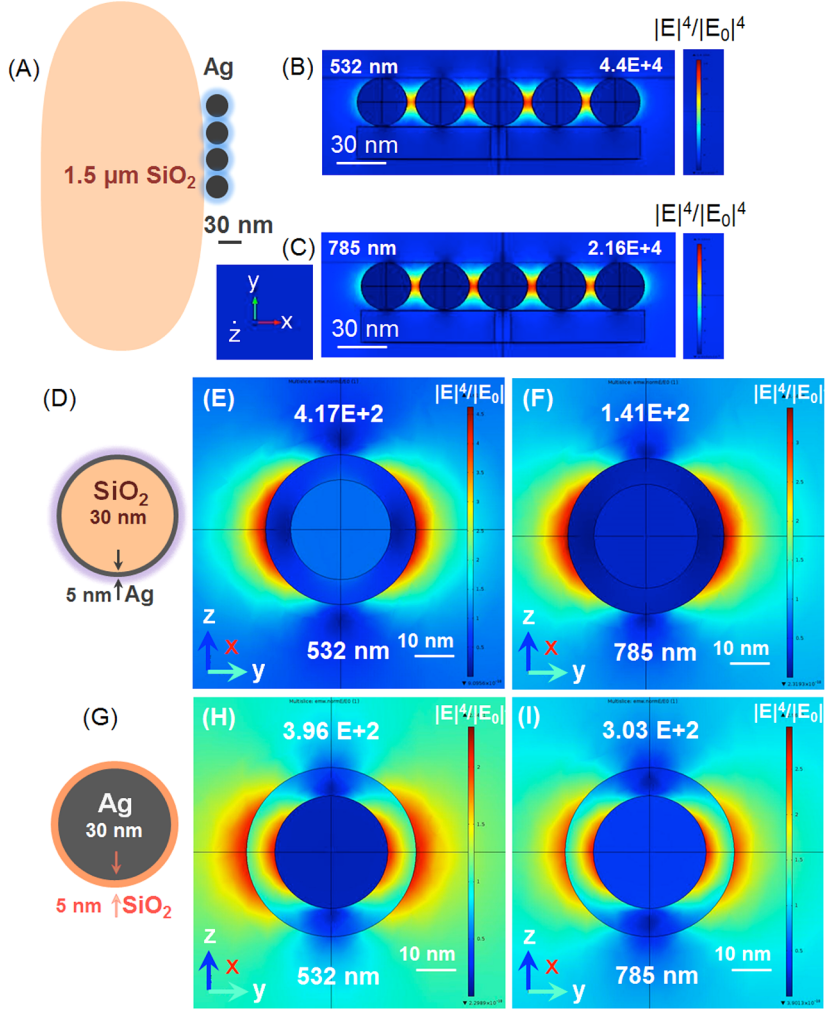

Figure 2. Calculated electric field distribution around particles with different configurations: (A−C) silver nanoparticles (30 nm) adsorbed on the surface of a silica microparticle (1.5 μm); (D−F) silica nanoparticle (30 nm) with a thin outer silver layer (5 nm) and (G−I) silver nanoparticle (30 nm) with a thin silica outer layer (5 nm). In the first configuration the electromagnetic field propagates with either a 532 nm or a 785 nm plane wave along *Y*-axis and has polarization along *X*-axis, the *Z*-axis is perpendicular to the *XY*-plane at the fixed interparticle distance (6 nm) (A−C). In the second and third configurations the electromagnetic field (532 or 785 nm) propagates along the *Z*-axis and each of them has polarization along the *Y*-axis, the *X*-axis is perpendicular to the *ZY*-plane (D−F and G−I). Insets with white numbers show peak values of the $|E|^4/|E_0|^4$ enhancement.

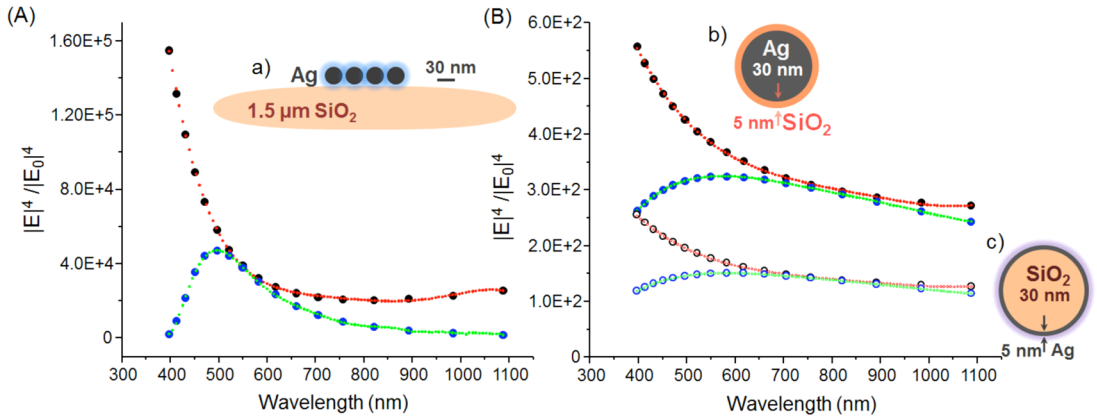

Figure 3. Electric field enhancement ($|E|^4/|E_0|^4$) scattered off the surface of silver nanoparticles with different configurations: (a) chain of silver nanoparticles (30 nm) adsorbed on the surface of silica microparticle (1.5 μm), (b) silver nanoparticles (30 nm) with a thin silica layer (5 nm) and (c) silica nanoparticles (30 nm) with a thin silver layer (5 nm). The values $|E|^4/|E_0|^4$ are in the wavelength range from 400 to 1100 nm (E_0 is the incident field amplitude). Dots are the calculated peak $|E|^4/|E_0|^4$ values: black dots show the whole *E* magnitude and blue dots show the *E* polarized along chosen *X*-axis (A) and *Y*-axis (B). Connecting lines are curve fits (red for full *E* value and green for the polarized *E* value): (a) $y = 3.76 \times 10^6 - 23010.69311x + 56.68135x^2 - 0.06957x^3 + 4.24 \times 10^{-5}x^4 - 1.03 \times 10^{-8}x^5$ and $y = 4.41 \times 10^8 - 6.03 \times 10^6x + 36085.97343x^2 - 123.92206x^3 + 0.26959x^4 - 3.86 \times 10^{-4}x^5 + 3.63 \times 10^{-7}x^6 - 2.17 \times 10^{-10}x^7 + 7.48 \times 10^{-14}x^8 - 1.13 \times 10^{-17}x^9$; (b) $y = 2.57 \times 10^3 - 10.06675x + 0.01731x^2 - 1.35 \times 10^{-5}x^3 + 3.98x^4$ and $y = -1777.51751 + 12.6822x - 0.03x^2 + 3.51 \times 10^{-5}x^3 - 2.06 \times 10^{-8}x^4 + 4.83 \times 10^{-12}x^5$; (c) $y = 1.15 \times 10^3 - 4.46x + 0.00763x^2 - 5.93 \times 10^{-6}x^3 + 1.74 \times 10^{-9}x^4$ and $y = -8.57 \times 10^2 + 6.02x - 0.01413x^2 + 1.64 \times 10^{-5}x^3 - 9.60 \times 10^{-9}x^4 + 2.24 \times 10^{-12}x^5$.

the surface of Ag-PVA NPs (separated at 6 nm distance) with either 532 or 785 nm in the direction of propagation along the *Y*-axis and has polarization along the *X*-axis (Figure 2B,C). The peak values of the electric part in the scattered field, $|E_x|^4/|E_0|^4$, (E_0 is the incident field) can be as high as $\sim 10^4$ with a twice higher magnitude at 532 nm (4×10^4) than at 785 nm (2×10^4).

To understand the electric part of the scattered field at the silica-silver interface at the nanoscale (<30 nm) we performed similar calculations for two spherical models (Figure 2D,G). The first one corresponds to a silica nanoparticle (diameter 30 nm) coated with a thin silver layer (5 nm) (Figure 2D, model II in Scheme 1). The second one has a reverse structure: silver nanoparticle (diameter 30 nm) with a thin silica layer (5 nm) (Figure 2G, model III in Scheme 1). In each of two configurations the incident electromagnetic field propagates along the *Z*-axis and has polarization along the *Y*-axis (Figure 2E,F and H,I). The peak values $|E_y|^4/|E|^4$ of the electric part in the scattered field are in the order of $\sim 10^2$ being 4 orders of magnitude higher at 532 nm than at 785 nm (Figure 2E,F) in the SiO_2@Ag-layer comparable to the Ag@SiO_2-layer at 532 nm (Figure 2H). The electric field enhancement in the Ag@SiO_2-layer is slightly less at 785 nm ($\sim 3 \times 10^2$) (Figure 2H) than at 532 nm (4×10^2) (Figure 2I); however, the latter is two times higher than in model II at 785 nm excitation (Figure 2F). In this way, for biological experiments, where longer excitation wavelengths are preferred, higher scattering electric field enhancement can be achieved rather on the silver nanoparticle surface than a thin solid nanolayer on the spherical curvature with diameter close to that of nanoparticles. However, this enhancement is below the limit for reliable SERS studies. Coupling of the electromagnetic field in the nanogaps (6 nm) of Ag NPs (model III) can increase the electric field by 2 orders of magnitude being only two times lower at 785 nm than at 532 nm.

In the range of excitation wavelengths from 400 to 1100 nm the highest values of the full electric field $|E|^4/|E_0|^4$ can reach the order of 10^5 (at 400 nm), followed by a nonlinear decay toward the longer wavelength region in the model I (Figure 3A). In contrast, the nonlinear $|E_x|^4/|E_0|^4$ decay curve exhibits a maximum peak around 500 nm with the tail of low enhancement in the near IR region (model I). In the region from 600 to 1100 nm the highest values are of the order of 10^4 falling to 10^3 in $|E_x|^4/|E_0|^4$ at 800 nm. The calculated peak values can be predicted from the fits to the polynomial curves with fifth (for $|E|^4/|E_0|^4$) and ninth (for $|E_x|^4/|E_0|^4$) order (model I, Figure 3A). In contrast, in two other models (II and III) the decay of the electric field enhancement ($\sim 10^2$) is slower and does not have a well-defined peak (Figure 3B). Over the whole wavelength range the electric field enhancement is about three times higher in model III than in model II being still in the order of 10^2. The calculated peak values at each wavelength can be predicted from the fit to the polynomial fits of the fourth ($|E|^4/|E_0|^4$) and fifth ($|E_x|^4/|E_0|^4$) order in both two models (Figure 3B), which are one and four orders lower than in the model I (Figure 3A).

To find out the contribution of only a silver or a silica surface to the total electric field enhancement, let us consider two additional models: (a) bare silver nanoparticles (Ag NPs) (Figure S4A,B) and (b) bare silica nanoparticles (SiO_2 NPs) (Figure S4C,D) with a diameter 30 nm. As in the previous calculation the incident

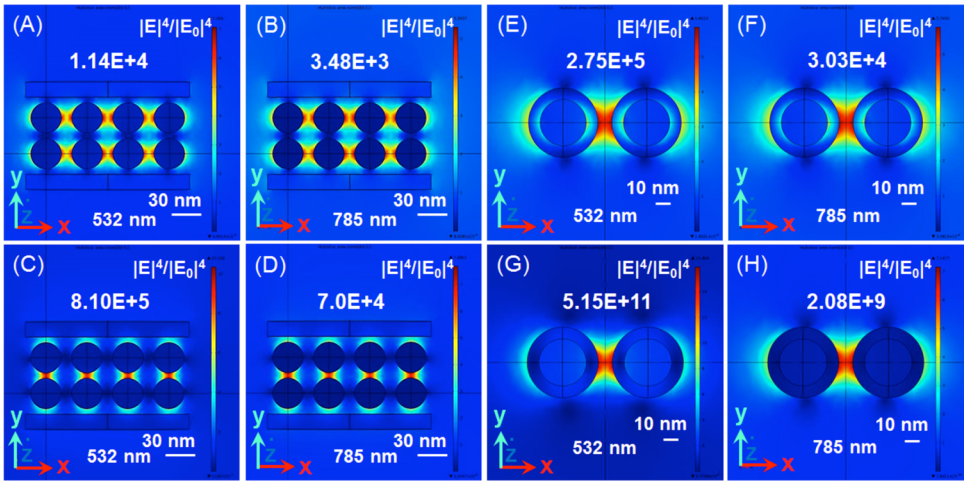

Figure 4. Calculated electric field distribution around dimers consisting of silver nanoparticles of different configurations: (A−D) silver nanoparticles (30 nm) adsorbed on the surface of silica microparticle (1.5 μm); (E,F) silver nanoparticle with a thin silica outer layer (5 nm); (G,H) silica nanoparticle (30 nm) with a thin outer silver layer (5 nm). Two incident electromagnetic plane waves (532 and 785 nm) propagate along the *Y*-axis and are polarized along the *X*-axis; the *Z*-axis is perpendicular to the *YX*-plane in the C−D configuration. In A−B, E−F, and G−H configurations the electromagnetic field has polarization along *Y*-axis and propagates along *X*-axis (*Z*-axis is perpendicular to the *XY*-plane). Insets with white numbers show peak values of the $|E|^4/|E_0|^4$ enhancement.

electromagnetic plane wave propagates along the *Z*-axis with polarization along the *Y*-axis and has 532 or 785 nm wavelength. The total electric field enhancement (*i.e.*, $|E|^4/|E_0|^4$) in bare Ag NPs is in the order of 10^2 with magnitudes twice higher at 532 nm (Figure S4A) than at 785 nm (Figure S4B). The contribution to the total electric field increase from the bare silica surface is of zero order with magnitudes of 5-fold increase almost indistinguishable at two selected excitation wavelengths (Figure S4C,D). In this way the silica surface can serve as a good insulator for the EM field increase providing a large surface area for intensified chemical interactions.

To understand the electromagnetic field distribution and find the high peak values beneficial for SERS studies let us extend our three models from monomers to dimers (the interparticle distance is 6 nm) (Figure 4). In the first dimer model I the calculated electric field enhancement depends on the direction of polarization (Figure 4A−D): 10^4 (at 532 nm) and 10^3 (at 785 nm) if the excitation wave propagates across the dimer structure with polarization along the *X*-axis (Figure 4A,B) and 10^5 (at 532 nm) and 10^4 (at 785 nm) in the reverse direction (Figure 4C,D). The inset numbers (white color) show higher values of the electric field increase at the shortest interparticle distance (nanogaps ≤2 nm). In the dimer of model III the SERS EF is being $\sim 2 \times 10^5$ (at 532 nm) and 3×10^4 (at 785 nm) at the shortest distance (nanogaps ≤ 2 nm) (Figure 4E,F). However, much higher electric field enhancement arises in the dimers of model II (Figure 4G,H) with the maximum $|E|^4/|E_0|^4$ values in the order of 5×10^{11} (at 532 nm) and 2×10^9 (at 785 nm). In the models II and III of dimers the incident electromagnetic wave propagates along the *Y*-axis with the polarization along the *X*-axis. These models are in agreement with our experimentally estimated values ($\sim 10^8$) taking into account short interparticle distances in dimers (<6 nm) and large surface area of silica microparticles. In this way, such high SERS EFs can be derived in models, which are comprised of silica with the outer silver film of various curvature and roughness (models in between in Figure 4C,D and Figure 4G,H and Figure 5B), in agreement with our previous studies.[20] To note, in the opposite case of the incident electromagnetic wave the electric field increase is lower. The higher values of the SERS enhancement factors at 532 nm excitation wavelength (one or 2 orders of magnitude) are in agreement with a two-step-process of the Raman radiation. In this context, the first excitation is proportional to the square of the local electric field $|E_{loc}(\omega_i)|^2/|E_0(\omega_i)|^2$ at the incident frequency, which can be higher at a longer frequency (shorter wavelength, closer to the silver absorption band). The second, the emitted Raman radiation can be enhanced by the metal particle resonance, which is proportional to the local electric fields at the Raman frequency, *i.e.*, $|E_{loc}(\omega_R)|^2/|E_0(\omega_R)|^2$. For this reason the difference in the SERS enhancement can be even higher according to the nonlinear increase of the electric field at the particle surface at very short distances (<10 nm).

We also calculated the decay of the electric field enhancement *versus* interparticle distance in all three models of these dimers (Figure 5A,B). The calculated data can be predicted from the exponential decay fits in all three models of dimers (532 and 785 nm) (Figure 5). The decay $|E|^4/|E_0|^4$ profiles are comparable for the dimers in the model I and model III (at 532 nm) being slightly lower at 785 nm (Figure 5A). In contrast, the $|E|^4/|E_0|^4$ field decays about 3-fold faster in the

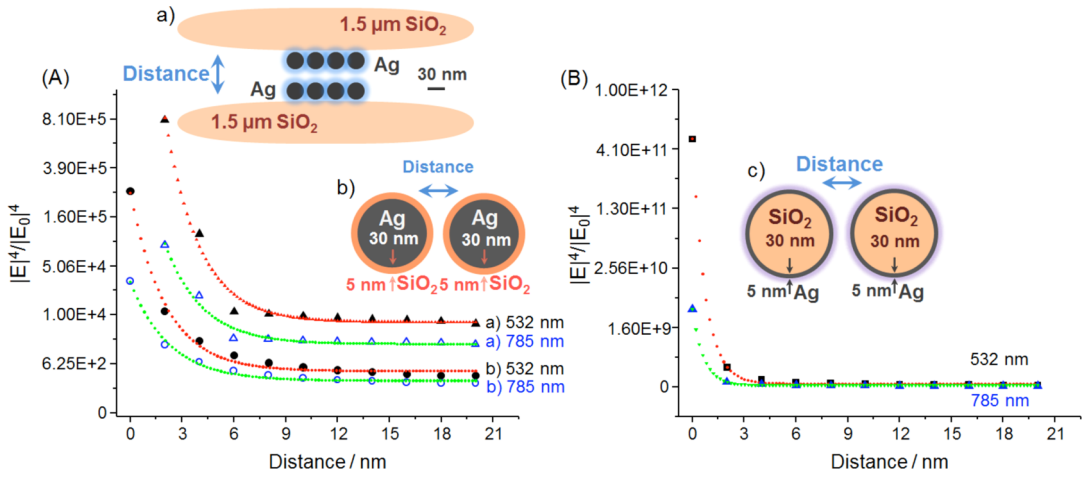

Figure 5. Calculated peak values of the electric field distribution in dimers consisting of silver nanoparticles of different configurations: a) chains of silver nanoparticles (30 nm) adsorbed on a silica microparticle (1.5 μm); b) silver nanoparticles (30 nm) with a thin silica outer layer (5 nm) and c) silica nanoparticle (30 nm) with a thin outer silver layer (5 nm). The calculated $|E|^4/|E_0|^4$ peak values are plotted *versus* distance in dimers with the first two configurations in A) and the third one in B) at two excitation wavelengths (532 and 785 nm) with the Y-polarization. Calculated data are represented with dots (triangles, circles and squares), which are connected by exponential fits: (a) at 532 nm $y = 9.26425 + 56.55241 \cdot \exp(-0.49819x)$ and at 785 nm $y = 7.03482 + 26.0206 \cdot \exp(-0.4655x)$ (b) at 532 nm $y = 4.27204 + 18.21968 \cdot \exp(-0.48909x)$ and at 785 nm $y = 3.27777 + 10.08513 \cdot \exp(-0.44492x)$; (c) at 532 nm $y = 10.81476 + 824.1175 \cdot \exp(-1.32587x)$ and at 785 nm $y = 5.51359 + 256.39735 \cdot \exp(-1.51973x)$.

model II of dimers with a slightly higher value (~1.53) at 785 nm than at 532 nm (~1.33) (Figure 5B). Higher values of the electric field enhancement can reach the order of 10^{11} or even 10^{12} at nanogaps <1 nm, which are far above the limit for single molecule detection at nonresonant conditions. However, such narrow nanogaps are difficult to achieve experimentally in spherical geometries.

Next we examined the influence of the curvature radius in the dimer of model II at the fixed interparticle distance 2 nm and an outer silver layer (5 nm) (Figure 6). The electric field $|E|^4/|E_0|^4$ enhancement rises with the increase of the radius in a nonlinear manner (fourth and second polynomial fits at 532 and 785 nm) (Figure 6). Nanoparticles should have at least 12 nm radius (for 532 nm excitation) and 22 nm (for 785 nm excitation) in order to overcome the threshold value of the electric field increase (~10^6). High electric field increase (10^9–10^{10}) can occur on the surface of nanoparticles with up to 30 nm radius (for 532 nm excitation) and 10^8 for 785 nm excitation.

Why does SERS need surface plasmons? When the incident radiation interacts with the surface, it causes the free electrons to oscillate with the incident electric field and polarizes the noble metal particles. This creates a strong local electric field at the particle surface known as a surface plasmon. When a molecule is in close proximity to a noble metal particle the molecule is polarized by the electric field of this particle (due to the interaction with the surface plasmon). This leads to an enhancement of the Raman signal, resulting in SERS. The enhancement originates, in part, from the interaction of the optical frequencies with the electric field of the plasmonic nanostructures. In this way SERS can suit

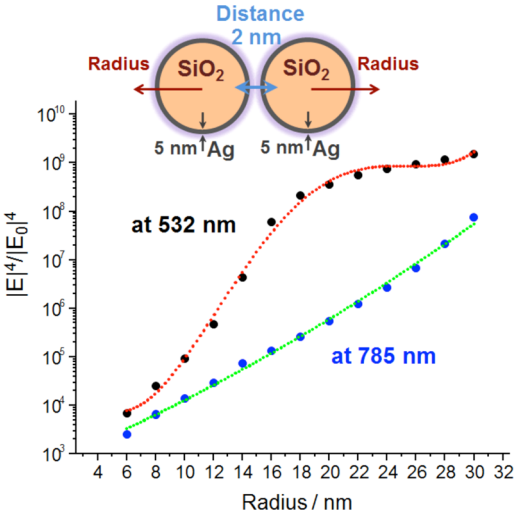

Figure 6. Calculated peak values of the electric field enhancement $|E|^4/|E_0|^4$ in homodimers consisting of two nanoparticles with a silica-core (various radii) and outer thin layer of silver (5 nm). The scattered field enhancement is determined for an incident electromagnetic plane wave with excitation wavelength either at 532 nm or at 785 nm at different radii of the nanoparticles. The circles indicate the calculated peak values of $|E|^4/|E_0|^4$, which are connected by polynomial fits: $y = 7.508 - 1.48288x + 0.18914x^2 - 0.00764x^3 + 1.02 \times 10^{-04}x^4$ (at 532 nm) and $y = 2.72425 + 0.12376x + 0.00145x^2$ (at 785 nm).

well to the study of polymer–metal composites since it enhances almost exclusively the first monolayer of molecules adjacent to the surface.[37]

SERS Spectra from Single Live NIH/3T3 Fibroblasts. Next SiO_2@Ag-PVA microparticles were embedded inside live NIH3T3 fibroblasts in order to collect SERS signatures of small biomolecules *in situ* (Figure 7). Optical phase contrast images show live fibroblasts with two

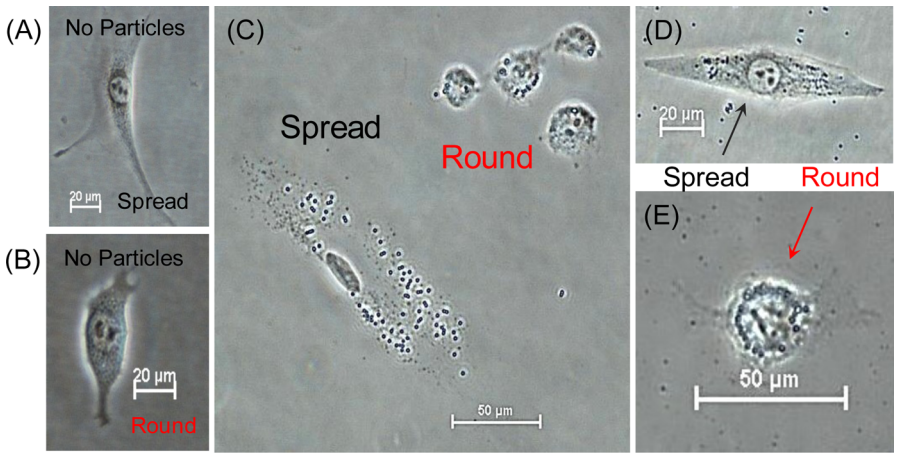

Figure 7. Optical phase contrast images of live NIH/3T3 fibroblasts with (A) spread or (B) round shapes (control, without any particles) and (C−E) those with embedded SiO_2@Ag-PVA MPs. Scale bars are 20 μm in A, B and D and 50 μm in C and E.

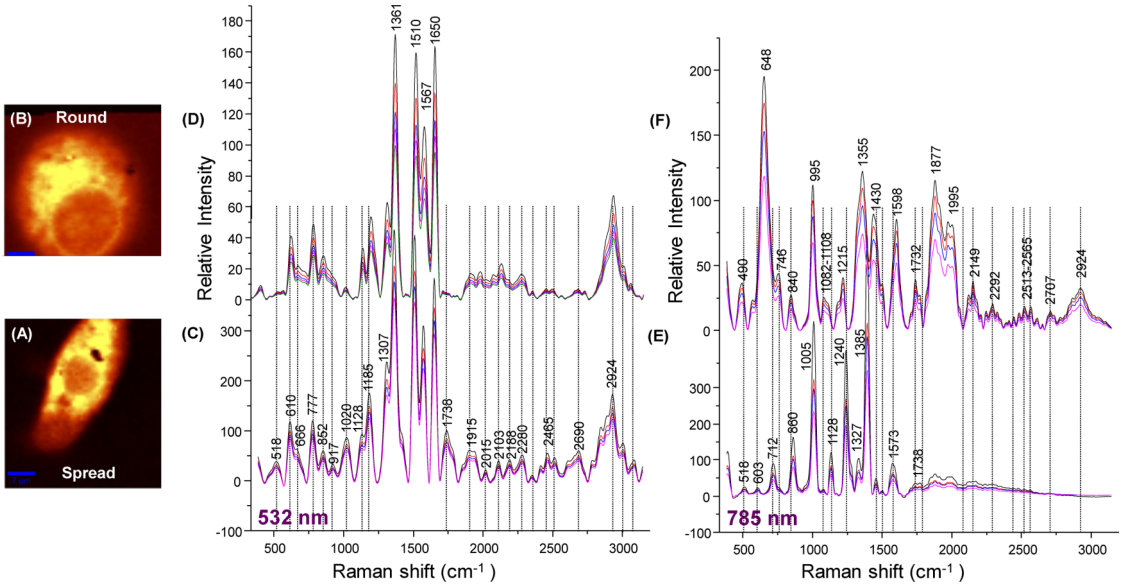

Figure 8. Raman spectroscopic images of single live NIH/3T3 fibroblasts with (A) spread (healthy, scale bar is 7 μm) and (B) round (unhealthy, scale bar is 5 μm) shapes. Raman assisted SERS images are constructed by integration of the overall intensity of Raman peaks of the intensity of the strongest bands in the region from 1000 to 2000 cm^{-1}. Bright areas in the images indicate areas of high SERS activity. (C−E) SERS spectra, which are collected from the cytoplasm at the areas of higher intensity (averaged over at least ten single cells). At 532 nm the grating was 600 g mm^{-1} (BLZ = 500 nm) with spectral resolution of 3 cm^{-1} and at 785 nm the grating was 300 gr mm^{-1} (BLZ = 750 nm) with spectral resolution of 6 cm^{-1}. The lower row shows SERS spectra from single healthy cells (spread shape), while the upper one shows SERS spectra from single unhealthy cells (round shape).

shapes: spread or round, which become more a needle-like or a sphere with embedded particles (Figure 7C−E).

Raman spectroscopic images of single live NIH/3T3 fibroblasts with spread or round shapes show bright areas due to the enhanced SERS activity from embedded SiO_2@Ag-PVA microparticles (Figure 8A,B). Overall SERS spectra were collected from within the cytoplasm (bright areas) and averaged over ten single live cells at 532 nm (Figure 8C,D) or 785 nm (Figure 8E, F) excitation wavelengths. The shape profile of the SERS spectra from spread or round live cells does not differ much at 532 nm. However, the intensity of strong SERS peaks (*e.g.*, 1350, 1504 or 1640 cm^{-1}) is about 3-fold higher (*i.e.*, 2.95, 3.1 or 2.5) from spread cells than from those with round shape. To note, in the absence of microparticles Raman spectra (from cytoplasm) do not exhibit distinct lines, but small broad peaks around 455 cm^{-1} (polysaccharides) or 915 cm^{-1} (glucose) and a larger one at 1365 cm^{-1} with a broad tail up to 2000 cm^{-1} (guanine, tryptophan, CH, CH_2 or CH_3 lipids) (Figure S5).[38] At higher excitation power the underlying background elevates with the increase of the peak intensities.

At 785 nm excitation wavelength the SERS shape profiles are different comparing spread or round single

TABLE 1. Assignment of SERS Spectral Bands (cm^{-1}) from Single Live NIH3T3 Fibroblasts at 532 or 785 nm Excitation Wavelengths

532 nm			785 nm	
spread	round	assignment/reference[a]	spread	round
518		ν(S—S)/31	518	
610	615	Cholesterol/42	603	
666	658	C—S stretching mode of cystine/24, 31		
		C—C tyrosine/23, 31	712	648
		T ring DNA,RNA bases/72		746
		Tryptophan sym./17, 24, 31	756	
777	770	Phosphatidylinositol/42		
852	846+tail	Tyrosine, glycogen, glucose/72, 65, 23	860	840
	1008	Phenylalanine/72	1005	
1020	1008	C—O ribose/78	1005	995
917		C—C glucose/42, 23, 24		
1128	1082—1108	C—O carbohydrates, C—N proteins, amide III/73	1128	1128
1185	1183	Cytosine, guanine, adenine/23	1171	1178
		Thiamine, adenine (DNA, RNA), amide III/72, 23	1240	1215
1307	1300	CH_2, CH_3 lipids, collagen/31		
		CH_2, CH_3 nucleic acids/67	1327	
1361	1350	Guanine (N_7)/62		1355
		CH_3 band/23	1385	
1453	1430	Deoxyribose/62		1434—1452
1510	1504	Cytosine/62		
1567	1564	Tryptophan/45		
		Guanine, adenine/23	1573	
		C═N, C═C quinoid ring/59	1598	
1650	1640	Amide I/92		
1738	1709—1779	Lipids C═O/3	1738	1732
1900—2000		C—N stretch/61	1900—2000	
2280	2271	C—N (triple bond)/16	2160	2292
	2513—2562	ν(S—H)/39	2550—2600	2550
2700	2707	C—H/16	2700	2730
2924	2924	OH, CH	2924	2924

[a] The cited references can be found in ref 37.

cells (Figure 8E,F). Although the number of peaks is higher from the round cells, the intensity of strong SERS peaks is 4-fold (*e.g.*, 1005 and 995 cm^{-1}) or 5-fold (1385 and 1355 cm^{-1}) higher from the spread cells. Overall, the intensity of SERS peaks is higher from spread cells than from those with round shape at either 532 or 785 nm excitation wavelengths.

(a). Detection of Amide I. No bands of amide I (1640—1650 cm^{-1})[39] were observed from any cells at 785 nm (Table 1). However, each of the single cells at 532 nm excitation wavelength shows strong and narrow amide I peaks corresponding to an α helix structure with a 6-fold higher intensity from round cells (1650 cm^{-1}). To remind, amide I is commonly used as a marker for the interpretation of the secondary protein structure, as the spectral overlapping with other functional groups can be avoided. The appearance of the amide I Raman band does not correlate with the protein aggregation state, but is determined by the size of the amino acid side chain.[40] The positions of the amide bands depend on the conformation of the polypeptide backbone and intra- and intermolecular hydrogen bonds, which are correlated to the protein secondary structure. Moreover, the position and intensity of the amide I band has been utilized to describe the structural organization of insulin fibrils[41] and globular proteins.[42,43] The absence of the amide I band at 785 nm is unlikely caused by a parallel orientation of all the peptide bonds[44] and is not due to protein aggregation, but may be due to poor specific adsorption of the peptide bonds to the metal particles.[45,46] In this way, this band can be easier detected at the higher excitation wavelength, which is closer to the UV—vis absorbance of silver (532 nm) than at 785 nm. Another reason could be in the difference of the size of the amino acid chain of amide I: the longer side chain increases the distance between the peptide bond and the particle surface preventing their immediate contact. As a result the contribution of the chemical contribution to the SERS enhancement mechanism may be probed: the surface enhancement occurs due to a short-range chemical mechanism in contrast to pure EM enhancement in live single cells.

To remind, the amide I band arises mainly from the C═O stretching mode of the peptide bond with minor contributions from the C−N stretching and N−H bending modes.[39−43,48] The amide I band is sensitive to the hydrogen-bonding pattern within a polypeptide because of the coupling between C═O and N−H bonds. Changes in the position of the amide I band indicate different secondary structures such as β-sheet (<1630 cm^{-1}) or α-helix (1650−1670 cm^{-1}). In our SERS spectra the amide I bond is detected at 1650 cm^{-1} (spread cells), indicating the presence of only α-helix structure. A mixture of β-sheet and α-helix structures can be present when the shape of the cell becomes round (1640 cm^{-1}). To note, the transition from the single α-helix to the mixture of both α-helix and β-sheet occurs through random coils (at 1647 cm^{-1}).

To note, SERS spectra from amide III bands can be detected as random coils from spread single live cells (1240 cm^{-1}, at λ_{exc} = 785 nm) followed by a significant shift (1215 cm^{-1}) as the shape becomes round (Table 1). To note, the latter is close to the β-sheet structure (1229−1235 cm^{-1}). However, at 532 nm excitation wavelength Raman bands of amide III can be enhanced at higher frequency shifts with an α-helix structure (1300−1307 cm^{-1}) which is introduced by the presence of 40% $_{\upsilon}$(C−N) stretch and 30% $_{\delta}$(N−H). This is in agreement with the SERS spectral signatures from amide I (described previously), indicating that spread cells contain random coils of α-helix structure. However, both α-helix and β-sheet structures can be present when the shape of live cells becomes round.

Amino acid residues such as tyrosine (840−860 cm^{-1}) and cystine (658 and 666 cm^{-1}), which constitute the small protein hormone insulin (can be taken as an example for the study of amide I) that is organized in two peptide chains linked by disulfide bridges can be also detected. SERS peaks from tyrosine appear from cells independently on the shape and excitation wavelength. However, the C−S stretching mode of cysteine arises as a small broad peak only at 532 nm. PVA as an anionic stabilizer does not increase the local concentration of tyrosine through hydrophobic and electrostatic interactions. There is a competition between tyrosine and PVA to solubilize and/or incorporate into the Stern layer by electrostatic or chemical forces. However, PVA is more hydrophobic than tyrosine with the affinity to be located rather in the Stern layer, while tyrosine may be hydrophobically incorporated into the junction region of the Stern-Palisade layer due to the presence of the phenyl group. To note, the PVA-Ag complex exhibits Raman peaks at 646 cm^{-1} (666 cm^{-1}) γ-OH, 921 cm^{-1} (917 cm^{-1}) υ-C−C, 1039 cm^{-1} (1020 cm^{-1}) υ-NO_3, 1428 cm^{-1} δ-CH_2 and δ-OH, 2913 cm^{-1} (2924 cm^{-1}) υ-C−H (of CH_2) at λ_{exc} = 514 nm[46,47] (at λ_{exc} = 532 nm in our spectral data), indicating the presence of PVA on the silver nanoparticle surface. There are only two Raman bands at 921 cm^{-1} (917 cm^{-1}) υ-C−C and 1039 cm^{-1} (1020 cm^{-1}) υ-NO_3 at the excitation wavelength 785 nm. Raman shifts in our data are due to the connection of PVA monomers by hydrogen bonds which form long parallel chains. The polymer chains can move far apart and lead to the weakening of the hydrogen bonds yielding a shift of different vibrational modes of PVA.

The sharp peak from phenylalanine (1005 cm^{-1}, at 785 nm excitation wavelength) indicates that the benzene ring adopts a geometry that is either standing up or at least tilting with respect to the particle surface (Figure 8E,F). However, this band is almost missing (1008 cm^{-1}) at 532 nm excitation wavelength, indicating that the benzene ring lies almost flat on the surface (Figure 8C,D). As there is no band at 1015 cm^{-1}, the tryptophan orientation (756 cm^{-1}) differs from that of phenylalanine. To note, the band from phenylalanine (around 1000 cm^{-1}) is independent of pH value. However, slightly acidic conditions (pH = 6) can be also detected in these cells due to the presence of 917 cm^{-1} from C−C glucose (round cells, at λ_{exc} = 532 nm), 1350−1360 cm^{-1} from guanine (independent of the shape and λ_{exc}) as well as 1564−1567 cm^{-1} from tryptophan (independent of the shape, at λ_{exc} = 532 nm). Moreover, the appearance of the following bands mostly at λ_{exc} = 532 nm indicates 3-fold lower pH values (pH = 2): 610−615 cm^{-1} from cholesterol, 777−770 cm^{-1} from phosphatidylinositol, 1307−1300 cm^{-1} from CH_2 and CH_3 lipids, 1510−1504 cm^{-1} from cytosine (Table 1).[48] Most of them are detected at lower Raman frequency shifts from the cells with round shapes, the only exception is cholesterol.

(b). Detection of Cholesterol. SERS detection of cholesterol is a very important aspect in diagnostics of live cells. To remind, cholesterol consists of a sterol (lipid molecule) and is an essential structural component of cell membranes that is required to maintain both membrane structural integrity and fluidity. The OH group on cholesterol interacts with the polar head groups of the membrane phospholipids, while the bulky steroid and the hydrocarbon chain are embedded in the membrane alongside the nonpolar fatty-acid chain of the other lipids. Moreover, cholesterol reduces the permeability of the plasma membrane to neutral solutes, H^+ ions and Na^+ ions.

The SERS peak from cholesterol can be detected as a relatively strong band at λ_{exc} = 532 nm from live cells (610 cm^{-1}). As the shape becomes more round the band is slightly shifted at 615 cm^{-1}, and the intensity decreases by 3-fold with development of a shoulder (666 cm^{-1}) (C−S stretching mode of cystine) (Table 1). The shoulder in Raman (SERS) lines with higher or lower intensity is due to the difference in the scattering geometry (symmetry of scattered light): A, B or E modes and selection rules.[45,48] The shoulder development may indicate changes in shape or

polarization properties of the Ag-PVA complex (described below).

Overall, we observed the development of a shoulder of strong SERS peaks mostly from round live cells (Figure 8D,F). These bands can be called overtone and combination bands, resulting from the effect of anharmonic terms in the potential energy. Overtone bands appear at approximately $2\upsilon_i$, where *i* is one of the fundamental modes. Combination bands appear at approximately $\upsilon_i + \upsilon_j$ where *i* and *j* are fundamental modes. The overtone and combination bands are always weaker than the corresponding fundamental modes. Methods of symmetry analysis can help determine which overtones might be allowed. Detailed analysis will be carried out in our further studies, excluding this work.

Significant spectral differences of lipids compared to cholesterol are observed around 2924 cm^{-1}.[49] This region is of specific interest in view of an erythrocyte membrane lipid (in diabetes mellitus, type II), because it is continuously exposed to the high blood glucose, leading to damage in structural components. In general, the increase of the relative Raman intensity of this peak indicates lipid damage in diabetic cells.[50] The Raman intensity increase of peaks from cholesterol is very typical for diabetic cells (increased cholesterol content is an important feature in diabetes). 2-Fold intensity increase at 2924 cm^{-1} is observed from the live cells with round shape (at $\lambda_{exc} = 785$ nm) (Figure 8C and D). To note, the appearance of these bands at lower intensity in the region from 2200 to 3000 cm^{-1} (in comparison to the overall high intensity of all SERS peaks) may be due to changes of the polarizability of the electric field vector, *e.g.*, from E^{para} to $E^{perpend}$ (Figure 8E). 3-Fold stronger SERS peaks (2924 cm^{-1}) are detected from spread cells at 532 nm excitation wavelength (Figure 8E,F). In this way, embedded SERS active SiO_2@Ag-PVA particles can differentiate the high risk of diabetes in either spread (3fold intensity increase) or round (2-fold intensity increase) live cells *in situ*.

(c). Detection of Glucose and Glycogen. In SERS spectra the Raman intensity increases with the amount of glucose.[51] Overall, characteristic SERS peaks from glucose are detected with higher intensity from spread live cells with a 6-fold (860 cm^{-1}, at 785 nm) and 2-fold (852 cm^{-1}, at 532 nm) increase in contrast to cells with round shape (840 cm^{-1}, at 785 nm) and (broad 846 cm^{-1}). In this way, spread live cells contain a greater amount of glucose than those with round shape. The range of the detected peaks can be also assigned to glycogen, which is a multibranched polysaccharide of glucose that serves as a form of energy storage in live cells. To remind, glycogen can be found in the form of granules in the cytoplasm (cytosol) in live cells, and plays an important role in the glucose cycle. Moreover, glycogen can be also responsible in the energy metabolism based on the observed changes of the cells.[52] During the cell growth the glycogen band intensities increase, meaning that the "healthy" or "unhealthy" state of live cell may depend on glycogen metabolism.

(d). Detection of Nucleic Acid. Overall, the SERS spectra from DNA (RNA), adenine and guanine are detected with higher intensity from spread live cells. The intensity increase is at least 2-fold higher at 785 nm excitation wavelength than at 532 nm (Figure 8C−F). In details, SERS peaks of guanine and adenine appear with a 3-fold higher intensity from spread cells (1185 cm^{-1}) than from round cells (1183 cm^{-1}) at 532 nm, but with a 5-fold increase at 785 nm. Raman bands of adenine (1240 and 1215 cm^{-1}) are enhanced by 10-fold from the spread live cells (at 785 nm), while the SERS signature of guanine (N_7) at 1361 and 1350 cm^{-1} is increased by 3-fold (at 532 nm).

Higher increase of Raman intensities of guanine (G) and adenine (A) is due to stronger interaction between amines and Ag NPs, *i.e.*, with the exocyclic nitrogen present in these bases.[53] Thymine (T) lacks this exocyclic amine group (NH_2) and interacts weakly with Ag NPs. A Ag-PVA nanofilm can enhance the Raman peaks of guanine, adenine and thymine with the following increase order G > A > C > T with a SERS enhancement factor of $\sim 10^8$ (at 785 nm).[52] The interaction of Ag-PVA with G and A is stronger *via* the intra-annular nitrogen atoms (in T there is only one nitrogen atom, the attachment is weaker). To note, in double-stranded DNA, the number of adenine is equal to the number of thymine and the number of guanine is equal to the number of cytosine. However, according to the order of the SERS intensity fall, *i.e.*, G > A > C > T, the difference of the number of DNA bases in DNA molecule does not play an important role in SERS intensities, but can be explained by different binding between DNA bases and Ag NPs. It is related to the adsorption abilities of the DNA bases with silver surface and the interactions between them.

The most likely orientation of guanine at the silver surface is with the $H_2N-C_8-N_9-C_4-N_3$ side of the molecule directed toward the metal surface.[54] Adenine can be adsorbed on the surface of Ag-PVA NPs with the $H_2N-C_8-N_9-C_4-N_3$ side and through the N_9 atom. The N_9 atom is the most suitable site also for guanine adsorption on a silver surface (from DFT calculations). For cytosine (C−N) the proximity of N_1 and N_5 atoms to the silver surface can be most probable.[55] These vibrations are in-plane and their high intensities may be due to a nonplanar orientation of the molecule on the silver surface, as is established by selection rules of the SERS effect.[56] The SERS spectral shifts of the adenine and guanine indicate a charge transfer at the Ag-PVA surface (from DFT calculations). The higher intensity increase of the SERS peaks at 785 nm can be due to resonance with the transition energies at the first excited state (764 nm) for the adenine-Ag complex, which is a charge transfer excited state. For the

guanine-Ag complex, the energy of the incident light at 785 nm is higher than the electronic transition energy of guanine-Ag (983 nm). Therefore, the experimental spectra with 785 nm incident light should be from enhanced Raman scattering.

Tyrosine can be also detected by SERS active Ag-PVA particles in single live fibroblasts (Table 1). To remind, tyrosine is a nonessential most easily oxidized amino acid with three potential coordination sites (NH_2, −COOH, and −OH) and a polar side group, being involved in many protein oxidations. Amino and carboxyl groups undergo chemical transformations, while the side chain remains intact. To note, the tyrosine-Ag^+ redox system can be used in the growth of PVA-induced silver composites.[57] Moreover, detection of tyrosine is important as it can be involved in several genetic metabolic disorders, including phenylketonuria,[58,59] tyrosinaemia type II and tyrosinosis.[58]

In contrast to tyrosine, phenylalanine has no other polar functional group to attract nearby Ag NPs, leading to weak SERS signals (Table 1). However, the phenylalanine and tyrosine residues each have group modes, A_1 and A_g[43] with polarizability components in all directions.[59] Therefore, these modes should be enhanced regardless of the orientation of the ring, which is Raman active. The other groups of modes can be enhanced in particular orientations. For example, the B_1 and B_{2g} modes can be enhanced if the face of the ring is tilted toward the metal's surface due to their polarizability in the *xz* direction of the ring (685 cm^{-1}), which is detected in the region 648−712 cm^{-1} (Table 1). The B_2 and B_{3g} (1585 cm^{-1}) can appear if the edge of the ring is tilted toward the surface due to their polarizability in the *yz* direction (not observed in our data, Table 1). Similarly the 828 cm^{-1}, which is characteristic of tyrosine (B_{1g}) and is rarely observed in SERS, was not detected in our data (Table 1 and Figure 8C−F).

It is important to note that the tyrosine bands are caused by Fermi resonance between the in-plane breathing mode of the phenol ring and an overtone of out-of-plane deformation mode. The intensities of these bands depend on the hydrogen bonding condition of the phenol side chain. For analytical studies the intensity ratio of 850 cm^{-1}/830 cm^{-1} (or 840 cm^{-1}) is often estimated: (i) 6−7 (non-hydrogen bonding); (ii) 2−3 (strong OH group of tyrosine); (iii) 0−1 (tyrosine acts as a donor); (iv) 1−2 (the OH group serves both as an acceptor and a donor of a hydrogen bond). In our data the ratio of these bands is 6.1 (at 785 nm) and 2.2 (at 532 nm), indicating the dominance of the non-hydrogen bonding in spread cells with intense OH group of tyrosine.

CONCLUSIONS

In this work a SERS active nanofilm, which is composed of preformed silver−boron nanoparticles in the matrix of poly(vinyl alcohol) (Ag-PVA) adsorbed on the surface of silica microparticles (SiO_2@Ag-PVA nanofilm), was used for intracellular detection of small biomolecules from live single NIH3T3 fibroblasts in real time. By applying FEM analysis the SERS EF can reach 10^5 with higher values from 10^9 to 10^{11} in the silver layer of 5 nm thickness. Preformed silver nanoparticles require at least 15 nm radius in order to exhibit SERS EF greater than 10^7 as deduced from the finite element method (FEM) calculations of the nonlinear SERS increase. Shorter excitation wavelength (532 nm) facilitates faster SERS increase than the longer one (785 nm).

The SERS spectra from single live NIH3T3 fibroblasts can be distinguished when the shape changes from spread ("healthy") to round ("unhealthy") states with a spectral difference at either 532 or 785 nm excitation wavelength. The amide I conformation from a random coiled α-helix structure (spread cells) into the mixture of both α-helix and a β-sheet (round cells) can be examined rather at 532 nm than at 785 nm. Slightly acidic conditions (pH = 6) can be detected with a higher probability mostly at 532 nm.

As a great advantage cholesterol can be detected with a 3-fold higher intensity in spread cells and 2-fold higher intensity in round cells, important for diabetes diagnostics: the higher intensity−the higher the risk of diabetes. Greater amount of glucose can be also detected from spread cells: 2-fold at 532 nm and 6-fold at 785 nm, but also glucogen, which is responsible for cell growth and "healthy" state. Detection of tyrosine can be also examined by SiO@Ag-PVA nanofilms and this is important in several genetic metabolic disorders such as phenylketonuria, tyrosinaemia type II and tyrosinosis. These findings can be important for clinical studies and SERS development as a reliable medical diagnostic tool with a real application.

METHODS

Materials. Silver nitrate ($AgNO_3$, analytical grade, 99.8%) was purchased from Serva (Germany). Poly(vinyl alcohol) (PVA, fully hydrolyzed) was acquired by Alfa Aesar (Germany). Sodium borohydride ($NaBH_4$, 98%), 3-aminopropyltriethoxysilane (APTES), DMEM, gentamicin, glucose and phosphate buffered saline (PBS, bioperformance certified, suitable for cell culture) were purchased from Sigma-Aldrich Co. (Germany). Calf Serum was obtained from PAA Laboratories GmbH (Austria). Silica particles (SiO_2, 1.55 ± 0.04 μm, 50 mg mL^{-1}) were obtained from Microparticles GmbH (Germany). Methanol was purchased from Merck KGaA (Germany) and toluene was obtained from AppliChem (Germany).

The water used in all the experiments was prepared in a three-stage Millipore Milli-Q Plus 185 purification system and had a resistivity higher than 18.2 MΩ cm^{-1}. For the experiments with living cells Milli-Q water was autoclaved.

Formation of Silver Nanoparticles in Aqueous Solution. Silver nanoparticles (Ag NPs, 30 nm diameter) have been produced by

chemical reduction of silver nitrate using sodium borohydride as a reducing agent in aqueous solution without organic stabilizers. The detailed procedure of formation of silver colloidal solution can be found elsewhere.[27] Briefly, a 1×10^{-3} mol L^{-1} concentration of $AgNO_3$ solution (room temperature) was mixed with fresh, ice-cold 1×10^{-3} mol L^{-1} or 3×10^{-3} mol L^{-1} sodium borohydride aqueous solution at a volume ratio 1:2 in a 0.25 L Erlenmeyer flask under vigorous stirring (600 rpm) at nitrogen atmosphere. In the first 20 s, the mixture turned bright yellow. After complete injection (less than 2 min) of silver nitrate solution, stirring was stopped immediately. The final solution of the colloidal mixture appeared with a clear yellow color and was kept in darkness to avoid the influence of light at 4 °C. No sediment of silver nanoparticles was observed within several months. The concentration of silver nanoparticles was estimated from the UV−vis absorbance spectra by the Beer−Lambert−Bouguer law as 0.86 mol L^{-1} (pH = 9.2 at room temperature).

Preparation of Aqueous Solution of Poly(vinyl alcohol) (PVA). Aqueous solution of poly(vinyl alcohol) was prepared with a typical concentration 2 mg mL^{-1} in 0.5 mol L^{-1} NaCl under vigorous stirring and heating at 70 °C for 30 min (pH = 6.5 at room temperature). The polyelectrolyte solution was purified in a sealed semipermeable membrane (cellulose acetate) against MQ water (MW cutoff 20 000 Da) and lyophilized.

Formation of Ag-PVA Nanofilms. Freshly prepared silver colloidal solution was added to aqueous solution of poly(vinyl alcohol) at a volume ratio 1:2, and the mixture was left for shaking overnight (350 rpm) in darkness. For stability the Ag-PVA mixture was incubated during mild shaking at 70 °C for 60 min in the Eppendorf Thermomixer compact (Hamburg, Germany) overnight. After incubation the Ag-PVA mixture was triply washed with MQ water followed by centrifugation at 14 000 rpm at 4 °C. Ag-PVA colloidal solution acquired a clear yellow color (pH = 8.3 at room temperature). The zeta potential of aqueous Ag-PVA colloidal solution was -17 ± 2 mV.

Preparation of Positively Charged Silica Microparticles. Before treatment the colloidal silica suspension (5 mg mL^{-1}) was triply washed with Milli-Q water by repetitive centrifugation at 8000 rpm. The initially negative zeta potential of silica (−22 ± 5 mV in pure water) was reversed by functionalizing the hydroxyl groups with aminosilanes.[28−30] 100 mg of silica particles were transferred from water to toluene by washing them twice with methanol followed with toluene by centrifugation at 8000 rpm for 5 min. The particles were then dispersed in 10 mL of toluene by stirring, and 1 mL of 3-aminopropyltriethoxysilane (APTES) was added dropwise under nitrogen atmosphere. The mixture was stirred for 1 h at room temperature. Positively charged silica particles were washed three times with toluene, methanol, and water consecutively in order to remove excess APTES and to transfer particles back into aqueous bulk. The washing of particles was carried out by centrifugation cycles at room temperature and 8000 rpm for 20 min. The zeta potential of the silica particles was +44 ± 5 mV.

Deposition of Ag-PVA Nanofilms on Silica Particles. Positively charged silica particles were added to aqueous solution of Ag NPs at a volume ratio 1:9 and incubated at room temperature for 15 min at mild shaking 300 rpm. The silica-silver mixture was triply washed with Milli Q autoclaved water by centrifugation (8000 rpm for 5 min). The adsorption procedure was repeated three times. The average zeta potential of the SiO_2@Ag-PVA particles was −25 ± 5 mV.

Theoretical Modeling of Electromagnetic Field Distribution of Different Silver Nanoshell Geometries by COMSOL Multiphysics Finite Element Method Simulation Software. The numerical simulations were performed with the commercial software package COMSOL Multiphysics (Version 4.3 with incorporated RF Module), which comprises electromagnetic code based on the Finite Element Method (FEM).

We examined six models to calculate the local electromagnetic field increase of the scattered plane wave of light (532 or 785 nm) off the silver-silica surface: (a) silver nanosphere with a diameter 15 nm and a surrounding silica layer with thickness 5 nm; (b) silica nanosphere with a diameter 15 nm and a surrounding silver layer with thickness 5 nm and (c) silica microsphere (diameter 1.5 μm) with adsorbed spherical silver nanoparticles (each with 30 nm diameter) and dimers of all three types of silver-silica particles. The incident electromagnetic field excites electric charges on the metallic surface and causes oscillations, which are intensified if at resonance with the surface plasmon field. The resonant oscillations radiate electromagnetic energy in all directions (*i.e.*, secondary radiation is a scattered field). The scattered electric field components were described by the Mie solution using Maxwell's equations and computed for the optical frequency range (from 2.76×10^{14} s^{-1} to 7.56×10^{14} s^{-1}). In this range silver can be modeled as a material possessing a complex relative permittivity with real, ε', and imaginary, ε'', components (*i.e.*, $\varepsilon_r = \varepsilon'(\lambda) + i\varepsilon''(\lambda)$, $\varepsilon'(\lambda) = n^2(\lambda) - \kappa^2(\lambda)$ and $\varepsilon''(\lambda) = 2\, n(\lambda)\kappa\lambda$) extracted from the complex refractive index.[31] The silver dielectric function was modeled using the Lorentz−Drude dispersion model:[32] The refractive index of the silica was taken from elsewhere.[33] The surrounding medium was defined as air. The nature of the interaction of the incident electromagnetic field (excitation plane wave) with the metallic surface (as a scattered field) has been considered at the silver-silica interface with different geometry and sequence of properties: metallic/dielectric and dielectric/metallic. In the study we employed a quasi-static approximation, for which silver nanospheres are much smaller than an optical wavelength with the incident electric field that is uniform over the dimensions of the particle.

In the frame of the RF module and FEM analysis (more suitable for near-field optics of interest) in COMSOL Multiphysics the wave vector, *k*, and electric field vector, *E*, are perpendicular to each other, and for calculation we selected *z* as the positive direction of the electromagnetic wave propagation. Differential equations determining the physics were defined by mesh points with increased density at high electromagnetic field concentration. A spatial mesh was interactively constructed to ensure that the E-field was properly solved at the position (0,0,0).

Each of six models was placed in the *yx*- or *zy*-plane in the middle of a sphere of air embedded in a perfectly matched layer (PML) domain, which acted as the boundary absorber of the scattered field, preventing any unwanted reflections in the domain. The PML layer was half the excitation wavelength in free space being outside the region of air with the thickness about 1/4 of the PML around the scattering model. The incident electromagnetic field was defined as a background being treated as plane waves with linear polarization according to the equation:

$$\Delta \times \mu_r^{-1}(\Delta \times E) - \kappa_0^2\left(\varepsilon_r - \frac{j\sigma}{\omega\varepsilon_0}\right)E = 0$$

where μ_r is the relative permeability, *E* is the electric field, κ_0 is the propagation wave vector ($\kappa_0 = 2\cdot\pi/\lambda$), ε_r is the complex relative permittivity, σ is the electrical conductivity, ω is the circular frequency and ε_0 is the vacuum permittivity.

For the scattered field formulation the background incident plane wave was defined as $E_{inc} = E_0 e^{-jk_0 z}x$ or $E_{inc} = E_0 e^{-jk_0 z}y$, which are electric fields with the electromagnetic plane wave propagating in the positive *z* direction and linear *x*-polarization or *y*-polarization (E_0 is the plane wave amplitude). The electric field enhancement factors for SERS were calculated as $|E_{peak}|^4/|E_{inc}|^4$ as a function of wavelength λ, where E_{peak} was the calculated relative electric field, *i.e.*, the scattered field generated by each model, and E_{inc} was the incident field. This approximation was derived from the knowledge that the Stokes Raman signal is proportional to the square of the local intensity of the electromagnetic field, the surface area and the Raman scattering cross section. The number of Stokes photons can be written as being

$$\text{pSERS} = \sigma_{ads}{}^{S}\frac{A}{A_0}\frac{|E_{loc}(\omega_i)|^2}{|E_0(\omega_i)|^2}\frac{|E_{loc}(\omega_R)|^2}{|E_0(\omega_R)|^2}$$

where σ_{ads}^{S} is the Stokes Raman cross section of the adsorbed molecule, A/A_0 is the ratio of the area of the structured surface to the area of the unstructured surface and the last (on the right)

term $(|E_{loc}(\omega_i)|^2/|E_0(\omega_i)|^2)(|E_{loc}(\omega_R)|^2/|E_0(\omega_R)|^2)$ describes the electromagnetic enhancement factor. The latter results from the enhancement of the Raman radiation in a two-step-process: first the excitation of Raman-active molecule is proportional to the square of the local electric field $|E_{loc}(\omega_i)|^2/|E_0(\omega_i)|^2$ at the incident frequency, which can be very high at the surface of metallic structures. The second, the emitted Raman radiation is enhanced by the metal particle resonance, which is proportional to the local electric fields at the Raman frequency, *i.e.*, $|E_{loc}(\omega_R)|^2/|E_0(\omega_R)|^2$). In most cases, the frequency of the Raman scattered light is close to that of the incident radiation so that the electromagnetic enhancement factor can be expressed as $|E_{loc}(\omega_i)|^4/|E_0(\omega_i)|^4$), *i.e.*, $|E_{peak}|^4/|E_{inc}|^4$ here.

Local electric field enhancements were calculated for the resonances at hot spots and examined *versus* radius of scatterers and the distance between their dimer structures.

The boundary conditions on the symmetry planes were the following:

(i) Symmetry in electric field:

$nxH|_{y=0} = 0$ and $nxH|_{x=0} = 0$ (condition of perfect magnetic conductor, PMC).

(ii) Symmetry in magnetic field:

$nxE|_{z=0} = 0$ (condition of perfect electric conductor, PEC).

Cell Culture and Incubation of Ag-PVA Nanofilms with Live NIH/3T3 Fibroblasts. Fibroblasts NIH/3T3 (purchased from DMSZ) were cultured in Dulbeco's modified eagle's medium (DMEM) supplemented with 4.5 g L^{-1} glucose, 10 vol % Calf Serum, 10^{-2} g L^{-1} Gentamicin (antibiotic). Cells were seeded with 3×10^3 cells cm^{-2} on the glass bottom dish (purchased from Greiner Bio One) 8.8 cm^2 culture surface and incubated (Binder) with 5% CO_2 at 37 °C overnight before Raman measurements.

SiO_2@Ag-PVA particles (400×10^{-6} L) were delivered into the cellular interior by internalization with endocytosis and transport into the late endosomes and lysosomes *via* overnight incubation in a 200×10^{-6} L culture medium suspension (5.34×10^4 cells) in the incubator. After electroporation the colloidal mixture with the cell suspension was mixed with 1×10^{-3} L of culture medium and deposited onto the glass bottom of a Petri dish in the incubator. The incubated cells were checked by optical phase contrast microscopy. Before Raman measurements the cells were washed at least three times with PBS aqueous solution.

Characterization. For size characterization of particles, a Zeiss EM 912 Omega transmission electron microscope (TEM) and a high-performance particle sizer (Malvern Instruments) for dynamic light-scattering (DLS) measurements were employed. Light absorption of particles was measured by a Varian CARY50 Conc. UV–vis spectrophotometer in the wavelength range from 200 to 900 nm in a quartz cell with 10 mm path length. The ζ-potential of particles was measured using a zeta sizer (Malvern Instruments). A Nikon Eclipse TS100 routine inverted microscope was employed to collect the refracted light from the transparent live cells through the enhancement of their phase contrast. Observation of the cell morphology was conducted by a Leica TCS SP inverted confocal laser scanning microscope system (CLSM Leica, Germany) equipped with a 40× oil immersion objective having 1.25 numerical aperture and 0.1 mm working distance.

Raman Spectroscopy and Microscopy. Surface enhanced Raman scattering (SERS) spectra were collected by a confocal Raman microscope alpha 300, WITec (Ulm, Germany) with a frequency doubled Nd:YAG (532 nm) laser excitation and piezoscanner (P-500, Physik Instrumente, Karlsruhe, Germany). A linearly polarized laser beam was focused through the LWD 20× and Nikon Fluor 60× water immersion objectives with numerical apertures NA = 0.40 and 1.00. The excitation laser intensity was kept in the range from 7.9 kW cm^{-2} to 23.8 kW cm^{-2} (*i.e.*, laser power from 1 mW to 3 mW) as measured by a Newport optical power meter 1830-C. The scattered light was filtered with an analyzer (further polarizer) through the confocal microscope pinhole. The spectra were acquired with a thermoelectrically cooled CCD detector (DU401A-BV, Andor, UK), with an integration time 1 s of 50 accumulations with a grating 600 g mm^{-1} (BLZ = 500 nm) and spectral resolution of 3 cm^{-1}. The signal-to-noise ratio was high enough to ensure the low value of the root-mean-square fluctuations averaged in time (typically below 5%). Basic alignment was carried out by a Raman spectrum of a silicon wafer with a characteristic Si line at 520 cm^{-1} during integration times from 0.3 to 1 s.

The SERS measurements of live cells were conducted in real time in a μ-dish (35 mm, Ibidi, Munich, Germany) equipped with a heating stage and external temperature probe (Bioscience Tools, USA) to maintain a temperature of 37 °C for the cells. The acquired SERS spectra were corrected for the baseline, background of the μ-dish substrate and the SiO_2 (485 cm^{-1} band). For imaging integration time of 0.1 s per pixel was used. The Scan Ctrl Spectroscopy Plus software (version 1.38, WITec) was used for measurement, WITec Project Plus (version 2.02, WITec) for spectra processing. Raman images were generated with the WITec software using a sum filter, which integrates the intensity of the signal for a defined wavenumber range of interest and subtracts the background as a linear baseline from the upper to lower border.

Conflict of Interest: The authors declare no competing financial interest.

Acknowledgment. We thank Rona Pitschke and Heike Runge (Department of Colloids at MPI) for electron microscopy analysis. The help with the cell culture assistance by Christine Pilz (Department of Biomaterials at MPI) is greatly appreciated. The financial support from the Max-Planck society and the Deutsche Forschungsgemeinschaft is acknowledged.

Supporting Information Available: UV–vis absorbance spectra of silver–boron nanoparticles in the matrix of poly(vinyl alcohol) (Ag-PVA) at different temperatures, SEM images of colloidal silica before and after adsorption of Ag-PVA nanofilm, UV–vis absorbance spectra of Ag-PVA nanoparticles before and after adsorption on colloidal silica at room temperature in water, calculated electromagnetic field increase in bare silver or silica nanoparticles (diameter 30 nm) and Raman spectra of single live NIH3T3 fibroblasts at different laser power excitation. This material is available free of charge *via* the Internet at http://pubs.acs.org.

REFERENCES AND NOTES

1. Knight, M. W.; Halas, N. J. Nanoshells to Nanoeggs to Nanocups: Optical Properties of Reduced Symmetry Core-Shell Nanoparticles Beyond the Quasistatic Limit. *New J. Phys.* **2008**, *10*, 105006–105016.
2. Wei, H.; Xu, H. Hot Spots in Different Metal Nanostructures for Plasmon-Enhanced Raman Spectroscopy. *Nanoscale* **2013**, *5*, 10794–10805.
3. Cecchini, M. P.; Turek, V. A.; Paget, J.; Kornyshev, A. A.; Edel, J. B. Self-Assembled Nanoparticle Arrays for Multiphase Trace Analyte Detection. *Nat. Mater.* **2013**, *12*, 165–171.
4. Etchegoin, P.; Le Ru, E. C. A Perspective on Single Molecule SERS: Current Status and Future Challenges. *Phys. Chem. Chem. Phys.* **2008**, *10*, 6079–6089.
5. Lim, D.-K.; Jeon, K.-S.; Hwang, J.-H.; Kim, H.; Kwon, S.; Suh, Y. D.; Nam, J.-M. Highly Uniform and Reproducible Surface Enhanced Raman Scattering from DNA-Tailorable Nanoparticles with 1-nm Interior Gap. *Nat. Nanotechnol.* **2011**, *6*, 452–460.
6. Li, J. F.; Huang, Y. F.; Ding, Y.; Yang, Z. L.; Li, S. B.; Zhou, X. S.; Fan, F. R.; Zhang, W.; Zhou, Z. Y.; Wu, D. Y.; Ren, B.; Wang, Z. L.; Tian, Z. Q. Shell-Isolated Nanoparticle-Enhanced Raman Spectroscopy. *Nature* **2010**, *464*, 392–395.
7. DeVetter, B. M.; Sivapalan, S. T.; Patel, D. D.; Schulmerich, M. V.; Murphy, C. J.; Bhargava, R. Observation of Molecular Diffusion in Polyelectrolyte-Wrapped SERS Nanoprobes. *Langmuir* **2014**, *30*, 8931–8937.
8. Dong, W.-F.; Sukhorukov, G.; Möhwald, H. Enhanced Raman Imaging and Optical Spectra of Gold Nanoparticle Doped Microcapsules. *Phys. Chem. Chem. Phys.* **2003**, *5*, 3003–3012.
9. Alvarez-Puebla, R. A.; Contreras-Caceres, R.; Pastoriza-Santos, I.; Perez-Juste, J.; Liz-Marzan, L. M. Au@pNIPAM Colloids as Molecular Traps for Surface-Enhanced,

Spectroscopic, Ultrasensitive Analysis. *Angew. Chem., Int. Ed.* **2009**, *48*, 138–143.
10. Pazos-Perez, N.; Wagner, C. S.; Romo-Herrera, J. M.; Liz-Marzan, L. M.; Garcia de Abajo, F. J.; Wittemann, A.; Fery, A.; Alvarez-Puebla, R. A. Organized Plasmonic Clusters with High Coordination Number and Extraordinary Enhancement in Surface-Enhanced Raman Scattering (SERS). *Angew. Chem., Int. Ed.* **2012**, *51*, 12688–12693.
11. Braun, G. B.; Lee, S. J.; Laurence, T.; Fera, N.; Fabris, L.; Bazan, G. C.; Moskovits, M.; Reich, N. O. Generalized Approach to SERS-Active Nanomaterials *via* Controlled Nanoparticle Linking, Polymer Encapsulation, and Small-Molecule Infusion. *J. Phys. Chem. C* **2009**, *113*, 13622–13629.
12. Lin, W. A Durable Plastic Substrate for Surface-Enhanced Raman Spectroscopy. *Appl. Phys. A: Mater. Sci. Process.* **2011**, *102*, 121–125.
13. Lu, L.; Randjelovic, I.; Capek, R.; Gaponik, N.; Yang, J.; Zhang, H.; Eychmuller, A. Controlled Fabrication of Gold-Coated 3D Ordered Colloidal Crystal Films and Their Application in Surface-Enhanced Raman Spectroscopy. *Chem. Mater.* **2005**, *17*, 5731–5736.
14. Marques, P. A. A. P.; Nogueira, H. I. S.; Pinto, R. J. B.; Neto, C. P.; Trindade, T. Silver-Bacterial Cellulosic Sponges as Active SERS Substrates. *J. Raman Spectrosc.* **2008**, *39*, 439–443.
15. He, D.; Hu, B.; Yao, Q. F.; Wang, K.; Yu, S. H. Large-Scale Synthesis of Flexible Free-Standing SERS Substrates with High Sensitivity: Electrospun PVA Nanofibers Embedded with Controlled Alignment of Silver Nanoparticles. *ACS Nano* **2009**, *3*, 3993–4002.
16. Chuan-Ling, Z.; Kong-Peng, Lv.; Huai-Ping, C.; Shu-Hong, Yu. Controlled Assemblies of Gold Nanorods in PVA Nanofiber Matrix as Flexible Free-Standing SERS Substrates by Electrospinning. *Small* **2012**, *8*, 648–653.
17. Cabrera, F. C.; Aoki, P. H. B.; Aroca, R. F.; Constantino, C. J. L.; dos Santos, D. S.; Job, A. E. Portable Smart Films for Ultrasensitive Detection and Chemical Analysis Using SERS and SERRS. *J. Raman Spectrosc.* **2012**, *43*, 474–477.
18. Yu, W. W.; White, I. M. Inkjet-Printed Paper-Based SERS Dipsticks and Swabs for Trace Chemical Detection. *Analyst* **2013**, *138*, 1020–1025.
19. Radziuk, D.; Moehwald, H. Highly Effective Hot Spots for SERS Signatures of Live Fibroblasts. *Nanoscale* **2014**, *6*, 6115–6126.
20. Radziuk, D.; Schuetz, R.; Masic, A.; Moehwald, H. Chemical Imaging of Live Fibroblasts by SERS Effective Nanofilm. *Phys. Chem. Chem. Phys.* **2014**, *16*, 24621–24634.
21. Chandy, T.; Sharma, C. P. Prostaglandin-E1-Immobilized Poly(Vinyl Alcohol)-Blended Chitosan Membranes-Blood Compatibility and Permeability Properties. *J. Appl. Polym. Sci.* **1992**, *44*, 2145–2156.
22. Mallapragada, S. K.; Peppas, N. A. Dissolution Mechanism of Semicrystalline Poly(vinyl alcohol) in Water. *J. Polym. Sci., Part B: Polym. Phys.* **1996**, *34*, 1339–1349.
23. Paradossi, G.; Lisi, R.; Paci, M.; Crescenzi, V. New Chemical Hydrogels Based on Poly(vinyl alcohol). *J. Polym. Sci., Part A: Polym. Chem.* **1996**, *34*, 3417–3495.
24. Jegal, J.; Lee, K. Nanofiltration Membranes Based on Poly(vinyl alcohol) and Ionic Polymers. *J. Appl. Polym. Sci.* **1999**, *72*, 1755–1762.
25. Creighton, J. A.; Blatchford, C. G.; Albrecht, M. G. Plasma Resonance Enhancement of Raman-scattering by Pyridine Adsorbed on Silver or Gold Sol Particles of Size Comparable to the Excitation Wavelength. *J. Chem. Soc. Faraday Trans.* **1979**, *75*, 790–798.
26. Cant, N. E.; Critchley, K.; Zhang, H. L.; Evans, S. D. Surface Functionalization for the Self-Assembly of Nanoparticle/Polymer Multilayer Films. *Thin Solid Films* **2003**, *426*, 31–39.
27. Antipov, A. A.; Sukhorukov, G. B.; Fedutik, Y. A.; Hartmann, J.; Giersig, M.; Möhwald, H. Fabrication of a Novel Type of Metallized Colloids and Hollow Capsules. *Langmuir* **2002**, *18*, 6687–6693.
28. Badley, R. D.; Ford, W. T.; McEnroe, F. J.; Assink, R. A. Surface Modification of Colloidal Silica. *Langmuir* **1990**, *6*, 792–801.
29. Johnson, P. B.; Christy, R. W. Optical Constants of Noble Metals. *Phys. Rev. E: Stat., Nonlinear, Soft Matter Phys.* **1972**, *6*, 4370–4379.
30. Palik, E. D. *Handbook of Optical Constants of Solids*; Academic Press: San Diego, 1998.
31. Kitamura, R.; Pilon, L.; Jonasz, M. Optical Constants of Silica Glass from Extreme Ultraviolet to Far Infrared at Near Room Temperature. *Appl. Opt.* **2007**, *46*, 8118–8133.
32. Bunn, C. W. Crystal Structure of Polyvinyl Alcohol. *Nature* **1948**, *161*, 929–930.
33. Mahanta, N.; Valiyaveettil, S. *In Situ* Preparation of Silver Nanoparticles on Biocompatible Methacrylated Poly(vinyl alcohol) and Cellulose Based Polymeric Nanofibers. *RSC Adv.* **2012**, *2*, 11389–11396.
34. Homan, K. A.; Chen, J.; Schiano, A.; Mohamed, M.; Willets, K. A.; Murugesan, S.; Stevenson, K. J.; Emelianov, S. Silver-Polymer Composite Stars: Synthesis and Applications. *Adv. Funct. Mater.* **2011**, *21*, 1673–1680.
35. Porel, S.; Venkatram, N.; Narayana Rao, D.; Radhakrishnan, T. P. *In Situ* Synthesis of Metal Nanoparticles in Polymeric Matrix and Their Optical Limiting Applications. *J. Nanosci. Nanotechnol.* **2007**, *7*, 1887–1892.
36. Koenig, J. L. *Spectroscopy of Polymers*, 2nd ed.; Elsevier Science, Inc.: Amsterdam, 1999.
37. Movasaghi, Z.; Rehman, S.; Rehman, I. U. Raman Spectroscopy of Biological Tissues. *Appl. Spectrosc. Rev.* **2007**, *42*, 493–541.
38. Kurouski, D.; Postiglione, T.; Deckert-Gaudig, T.; Deckert, V.; Lednev, I. Amide I Vibrational Mode Suppression in Surface (SERS) and Tip (TERS) Enhanced Raman Spectra of Protein Specimens. *Analyst* **2013**, *138*, 1665–1673.
39. Dong, J.; Wan, Z.; Popov, M.; Carey, P. R.; Weiss, M. A. Insulin Assembly Damps Conformational Fluctuations: Raman Analysis of Amide I Linewidths in Native States and Fibrils. *J. Mol. Biol.* **2003**, *330*, 431–442.
40. Sane, S. U.; Cramer, S. M.; Przybycien, T. M. A Holistic Approach to Protein Secondary Structure Characterization Using Amide I Band Raman Spectroscopy. *Anal. Biochem.* **1999**, *269*, 255–272.
41. Pavan Kumar, G. V.; Ashok Reddy, B. A.; Arif, M.; Kundu, T. K.; Narayana, C. Surface-Enhanced Raman Scattering Studies of Human Transcriptional Coactivator p300. *J. Phys. Chem. B* **2006**, *110*, 16787–16792.
42. Podstawka, E.; Ozaki, Y. Bombesin-modified 6−14 C-terminal Fragments Adsorption on Silver Surfaces: Influence of a Surface Substrate. *Biopolymers* **2008**, *89*, 941–950.
43. Dollish, F. R.; Fateley, W. G.; Bentley, F. F. *Characteristic Raman Frequencies of Organic Compounds*; Wiley: New York, 1974.
44. Krimm, S.; Liang, C. Y.; Sutherland, G. B. B. M. Infrared Spectra of High Polymers. 5. Polyvinyl Alcohol. *J. Polym. Sci.* **1956**, *22*, 227–247.
45. Tobin, M. C. *Laser Raman Spectroscopy*; Wiley Interscience: New York, 1970.
46. Siesler, H. W.; Holland-Moritz, K. *Infrared and Raman Spectroscopy of Polymers. Practical Spectroscopy Series*; Marcel Dekker, Inc.: New York, 1980.
47. Lin, J.; Zeng, Y.; Lin, J.; Wang, J.; Li, L.; Huang, Z.; Li, B.; Zeng, H.; Chen, R. Erythrocyte Membrane Analysis for Type II Diabetes Detection Using Raman Spectroscopy in High-wavenumber Region. *Appl. Phys. Lett.* **2014**, *104*, 104102-1–104102-4.
48. Jain, S. K.; Mc Vie, R.; Duett, J.; Herbst, J. J. Erythrocyte-Membrane Lipid-Peroxidation and Glycosylated Hemoglobin in Diabetes. *Diabetes* **1989**, *38*, 1539–1543.
49. Tognalli, N. G.; Scodeller, P.; Flexer, V.; Szamocki, R.; Ricci, A.; Tagliazucchi, M.; Calvo, E. J.; Fainstein, A. Redox Molecule Based SERS Sensors. *Phys. Chem. Chem. Phys.* **2009**, *11*, 7412–7423.
50. Liu, R.; Zhang, D.; Cai, C.; Xiong, Y.; Li, S.; Su, Y.; Si, M. NIR-SERS Studies of DNA and DNA Bases Attached on Polyvinyl Alcohol (PVA) Protected Silver Grass-Like Nanostructures. *Vib. Spectrosc.* **2013**, *67*, 71–79.
51. Nath, S.; Ghosh, S. K.; Kundu, S.; Praharaj, S.; Panigrahi, S.; Pal, T. Is Gold Really Softer Than Silver? HSAB Principle Revisited. *J. Nanopart. Res.* **2006**, *8*, 111–116.

52. Giese, B.; McNaughton, D. Density Functional Theoretical (DFT) and Surface-Enhanced Raman Spectroscopic Study of Guanine and Its Alkylated Derivatives – Part 2: Surface-Enhanced Raman Scattering on Silver Surfaces. *Phys. Chem. Chem. Phys.* **2002**, *4*, 5171–5182.
53. Cortes, S.; Ramos, J. V. G. SERS of Cytosine and Its Methylated Derivatives on Metal Colloids. *J. Raman Spectrosc.* **1992**, *23*, 61–66.
54. Creighton, J. A. *Spectroscopy of Surfaces*; Wiley: Chichester, U.K., 1988.
55. Al-Thabaiti, S. A.; Obaid, A. Y.; Khan, Z. Synthesis of Poly(vinyl alcohol)-Silver Nanocomposites and Effect of CTAB on Their Morphology. *J. Nanomater. Mol. Nanotechnol.* **2013**, *2*, 7.
56. Schulze, A.; Kohlmueller, D.; Mayatepek, E. Sensitivity of Electrospray-Tandem Mass Spectrometry Using the Phenylalanine/tyrosine-Ratio for Differential Diagnosis of Hyperphenylalaninemia in Neonates. *Clin. Chim. Acta* **1999**, *283*, 15–20.
57. Huang, T.; Warsinke, A.; Kuwana, T.; Scheller, F. W. Determination of L-Phenylalanine Based on an NADH-Detecting Biosensor. *Anal. Chem.* **1998**, *70*, 991–997.
58. Deutsch, J. C. Determination of P-hydroxyphenylpyruvate, P-hydroxyphenyllactate and Tyrosine in Normal Human Plasma by Gas Chromatography-Mass Spectrometry Isotope-dilution Assay. *J. Chromatogr. B* **1997**, *690*, 1–6.
59. Ferraro, J. R.; Nakamoto, K. *Introductory Raman Spectroscopy*; Academic Press: Boston, MA, 1994.